Journal of Environmental Economics & Chemical Processes (JEECP)

https://doi.org/10.22034/jeecp.2026.2089220.1028

Journal Homepage: *WWW.JEECPJournal.com*

Journal of Environmental Economics & Chemical Processes (JEECP)

ORIGINAL RESEARCH PAPER

Magnetite-Loaded Zeolite A Derived from Iranian Kaolin through Template-Free Hydrothermal Synthesis for Oxidative Desulfurization of Real Gas Condensate

Fereshteh Abbasi Oghani [a]; Tahereh Mojtahed [b]; Alimorad Rashidi [c,*]; Kimia Shahbazi [d]

[a]*Department of Chemical Engineering, Science and Research Branch, Islamic Azad University, Tehran, Iran.*
[b]*Department of Chemistry, Science and Research Branch, Islamic Azad University, Tehran, Iran.*
[c]*Nanotechnology Research Center, Research Institute of Petroleum Industry (RIPI), Tehran, Iran.*
[d]*Department of Chemical Technologies, Iranian Research Organization for Science and Technology (IROST), Tehran, Iran.*

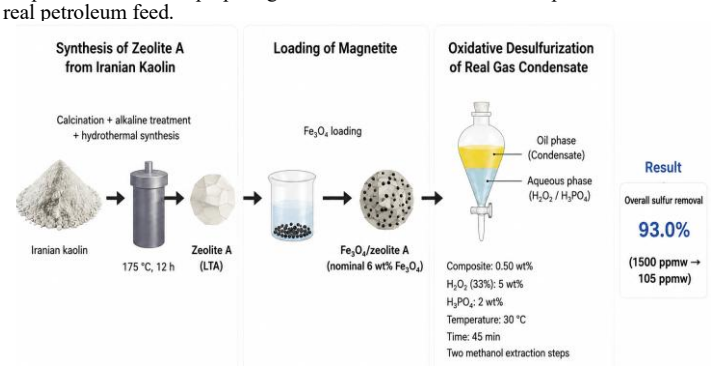
P A P E R I N F O

Paper history:
Received: 08/02/2026
Revised: 08/18/2026
Accepted in revised form: 08/18/2026
Published: 09/30/2026

Keywords:
Iranian Kaolin;
Zeolite A;
LTA Framework;
Magnetite;
Oxidative Desulfurization;
Gas Condensate;
Hydrogen Peroxide.

A B S T R A C T

Iranian kaolin was converted to zeolite A by template-free hydrothermal synthesis using industrial-grade raw materials. After calcination at 550 °C for 5 h and alkaline pretreatment, the hydrothermal mixture was crystallized at 175 °C for 12 h. Magnetite prepared by coprecipitation was subsequently deposited on the zeolite at a nominal loading of 6 wt% relative to the support. The resulting Fe_3O_4/zeolite A composite was characterized by powder X-ray diffraction, Fourier-transform infrared spectroscopy, nitrogen adsorption-desorption, and field-emission scanning electron microscopy. XRD showed the characteristic low-angle reflections of the LTA framework together with additional reflections consistent with a spinel iron-oxide phase. The BET specific surface area, external surface area, and total pore volume were 18.64 $m^2 g^{-1}$, 9.49 $m^2 g^{-1}$, and 0.03395 $cm^3 g^{-1}$, respectively. Oxidative desulfurization was evaluated with a real gas condensate containing 1500 ppmw sulfur. At the selected treatment condition (0.50 wt% composite, 5 wt% of 33 wt% H_2O_2 solution, 2 wt% H_3PO_4, 30 °C, and 45 min), followed by two methanol extractions, sulfur decreased to 105 ppmw. The corresponding 93.0% value therefore represents overall sulfur removal across the combined oxidation-extraction sequence. These results establish a practical route for preparing an LTA-based iron-oxide composite from Iranian kaolin and applying it to a real petroleum feed.



1. Introduction

Sulfur in petroleum fuels is associated with sulfur-oxide emissions, corrosion, catalyst deactivation, and loss of fuel quality. Hydrodesulfurization (HDS) remains the principal industrial route for sulfur removal, although its demand for hydrogen, elevated temperature and pressure, and sulfided catalysts becomes increasingly restrictive when deep removal of sterically hindered aromatic sulfur compounds is required [1-3]. Oxidative desulfurization (ODS) offers a different reaction pathway: organosulfur compounds are oxidized to more polar sulfoxides and sulfones that can subsequently be transferred from the hydrocarbon phase by extraction or adsorption [4]. The approach has also been investigated with sour gas condensate, providing a closer representation of industrial light petroleum streams than single-compound model fuels [5].

ODS performance is governed by the oxidant, catalyst chemistry, accessible surface, and mass transfer across the hydrocarbon/oxidizing-phase interface [4]. Transition-metal systems based on Mo, W, V, Ti, Co, Mn, Cu, and Fe have been examined alongside polyoxometalates, ionic liquids, porous carbons, metal-organic frameworks, and molecular sieves. Magnetite is particularly relevant because the inverse-spinel structure contains Fe^{2+} and Fe^{3+} sites capable of redox interaction with peroxide [6]. Fe_3O_4-containing materials have consequently been used as recoverable components in ODS formulations [7, 8], while incorporation of iron oxides into zeolitic solids can also modify handling and interfacial properties depending on loading and dispersion [9].

A porous aluminosilicate support can disperse a deposited phase while contributing an accessible external surface for adsorption and reaction. Zeolite

* Corresponding Author: Alimorad Rashidi
E-mail address: rashidiam@gmail.com
ISSN: 3116-0050
URL: https://www.jeecpjournal.com/article_735605.html

Please cite this article as: F. Abbasi Oghani, T. Mojtahed, A. Rashidi, & K. Shahbazi, *Journal of Enviromental Economics & Chemical Processes (JEECP)*, 2026, *3*(3), 153-157. https://doi.org/10.22034/jeecp.2026.2089220.1028

/© 2026 The Author(s). Published by Power of New Vision Movement Institute.

A, which has the LTA topology, combines a polar framework, ion-exchange capacity, and a regular micropore system and can be synthesized from alkaline aluminosilicate gels or from thermally activated kaolin [10–12]. Hydrothermal conversion of kaolin is attractive because the mineral already supplies both silicon and aluminum; microwave-assisted routes can shorten crystallization, although conventional hydrothermal treatment remains experimentally straightforward [13].

Template-free synthesis removes the need for an organic structure-directing agent and the associated template-removal step [10]. In kaolin-based routes, calcination first converts the clay to a more reactive aluminosilicate, after which alkaline dissolution and hydrothermal crystallization can yield the LTA phase [11,12]. The present work uses Iranian kaolin and industrial-grade domestic reagents as the synthesis inputs. Their local availability is relevant to material sourcing, whereas economic or environmental superiority would require separate cost and life-cycle assessments.

Here, Iranian kaolin was converted to zeolite A by a template-free hydrothermal route and then combined with Fe_3O_4 at a nominal loading of 6 wt% relative to the zeolite support. The composite was examined by XRD, FTIR spectroscopy, nitrogen adsorption-desorption, and FESEM, and its performance was assessed in an H_2O_2/H_3PO_4 oxidation step followed by methanol extraction of a real gas-condensate feed. Interpretation of the desulfurization data is based on the measured treatment sequence rather than on an isolated catalyst contribution.

2. Method

2.1. Methodology

Iranian kaolin (G-KS grade) was supplied by Parsian Mineral Chemical Co. (Iran). Industrial sodium silicate solution (water glass) was obtained from Ab Shisheh Zarrin, Qazvin, Iran. According to the supplier, the solution contained 42 wt% SiO_2, 21 wt% Na_2O, and 37 wt% H_2O, corresponding to a nominal SiO_2/Na_2O mass ratio of approximately 2:1 and a density of 1.4 g cm^{-3}. It was used as received. Supplier-reported compositions of the kaolin and sodium silicate solution are given in Tables S10 and S11, respectively.

Sodium hydroxide pellets, iron(II) chloride tetrahydrate ($FeCl_2{\cdot}4H_2O$), iron(III) chloride hexahydrate ($FeCl_3{\cdot}6H_2O$), aqueous ammonia, 33 wt% hydrogen peroxide solution, phosphoric acid, methanol, and distilled water were used without further purification. All chemical reagents were industrial grade and sourced in Iran. The petroleum feed was an industrial gas condensate with the properties listed in Table 1. Supplier data were used to calculate the nominal synthesis-batch composition; no independent bulk-composition analysis of the kaolin or sodium silicate was performed.

2.2. Template-Free Hydrothermal Synthesis of Zeolite A

Kaolin was calcined at 550 °C for 5 h and then treated with NaOH at a kaolin-to-NaOH mass ratio of 1:3. The alkali-treated material was washed thoroughly with distilled water and dried at 100 °C for 12 h. Because this preliminary NaOH was removed during washing, it was not included in the nominal composition of the subsequent hydrothermal batch.

For hydrothermal synthesis, 102 g of activated kaolin was dispersed in a portion of the distilled water. In a separate vessel, 20 mL of sodium silicate solution was diluted with distilled water and added gradually to the kaolin suspension under continuous stirring. A solution containing 40 g of NaOH in the remaining water was then introduced. The total amount of distilled water used for preparation of the synthesis mixture was 200 mL. On an oxide basis, normalized to Al_2O_3, the nominal batch composition was:

2.61 Na_2O: 1.00 Al_2O_3: 6.08 SiO_2: 53.3 H_2O

Only the NaOH introduced directly into the hydrothermal mixture was included in this calculation. The suspension was stirred for at least 3 h before transfer to a sealed autoclave and crystallization at 175 °C for 12 h under autogenous pressure. After cooling, the solid was recovered, washed thoroughly with distilled water, and dried at 100 °C for 12 h. A final calcination was carried out at 550 °C for 5 h. No organic structure-directing agent or hard template was used.

2.3. Magnetite Synthesis and Composite Preparation

Magnetite was prepared by aqueous coprecipitation of Fe^{3+} and Fe^{2+} salts at an approximate molar ratio of 2:1 [12]. $FeCl_2{\cdot}4H_2O$ (0.10 g) and $FeCl_3{\cdot}6H_2O$ (0.27 g) were dissolved in 30 mL of distilled water and stirred for 5 min. Aqueous ammonia (2 mL) was added dropwise under continuous stirring, producing a black precipitate. The suspension was maintained at 80 °C for 1 h, cooled, washed repeatedly with distilled water, and dried. For composite preparation, 0.06 g of the recovered Fe_3O_4 was introduced per gram of zeolite A. This preparative ratio corresponds to a nominal loading of 6 wt% relative to the support; the retained Fe content of the final composite was not quantified independently. Magnetite was dispersed in distilled water, zeolite A was added, and the slurry was stirred at 50 °C for 3 h. The product was dried at 100 °C for 6 h without further calcination and is denoted Fe_3O_4/zeolite A.

2.4. Oxidative Desulfurization and Sulfur Analysis

ODS experiments were carried out with a real industrial gas condensate containing 1500 ppmw total sulfur (Table 1). The use of an unmodelled petroleum feed retained the native hydrocarbon matrix and sulfur distribution encountered in a light industrial stream [5].

The composite was used without additional activation. Unless otherwise specified, reagent dosages were calculated relative to the initial mass of gas condensate. The selected oxidation condition consisted of 0.50 wt% Fe_3O_4/zeolite A, 5 wt% of the 33 wt% H_2O_2 solution, and 2 wt% H_3PO_4. Reactions were conducted at 30 °C for 45 min with stirring at 400 rpm. Agitation maintained contact among the hydrocarbon phase, aqueous oxidant-acid phase, and suspended solid and therefore influenced interfacial mass transfer [5].

Following oxidation, the hydrocarbon phase was extracted twice with fresh methanol. Each extraction used a methanol-to-initial-feed volume ratio of 1:1. After mixing and phase separation, the methanol-rich phase was removed before fresh solvent was added for the second stage. Total sulfur in the initial feed and treated hydrocarbon phase was measured by energy-dispersive X-ray fluorescence in accordance with ASTM D4294-24 [15]. Because sulfur was measured after extraction, the reported removal values describe the complete oxidation-extraction sequence rather than oxidation alone.

The oxidant-to-sulfur molar ratio (O/S) was calculated from the amount of H_2O_2 added and the total sulfur content of the initial feed. For a 100 g basis, 5 g of 33 wt% H_2O_2 solution contains 1.65 g H_2O_2 (0.0485 mol), whereas 1500 ppmw sulfur corresponds to 0.150 g sulfur (0.00468 mol). The resulting O/S ratio is 10.4. Complete oxidation of one mole of sulfur to the corresponding sulfone requires two moles of H_2O_2; excess peroxide is commonly applied because decomposition, competing reactions, incomplete utilization, and phase-transfer resistance reduce oxidant efficiency [16]. The calculation is provided in Supplementary Section S2. Sulfur removal was determined using Equation (1):

$$Sulfur\ removal\ (\%) = \left[\frac{C_{0,s} - C_{t,s}}{C_{0,s}}\right] \times 100 \qquad (1)$$

where $C_{0,S}$ and $C_{t,S}$ denote the initial and residual total sulfur concentrations, respectively, in the gas-condensate phase.

Table 1. Physicochemical properties of the real gas-condensate feedstock.

Property	Unit	Value
Density at 15 °C	g cm^{-3}	0.750
API gravity	°API	57.2
Initial total sulfur content	ppmw	1500
Equivalent sulfur content	wt%	0.150
Water content	vol%	<0.025
Salt content	PTB	<1
Kinematic viscosity at 20 °C	$mm^2\ s^{-1}$	1.10

2.5. Characterization

Powder X-ray diffraction was recorded on a Bruker AXS D8 Advance diffractometer using Cu Kα radiation. Data were collected from 5.0 to 69.7° 2θ with a step size of 0.02° and a counting time of 1 s per step. Phase identification relied on peak positions and the overall diffraction sequence; neither Rietveld refinement nor quantitative phase analysis was performed. Nitrogen adsorption-desorption measurements were obtained at 77 K with a PHS-1020 analyzer after degassing at 120 °C for 2 h. The BET fit covered P/P_0 = 0.1375-0.1881. External surface area and micropore volume were derived by t-plot analysis, total pore volume was taken near P/P_0 = 0.99, and the BJH pore-size distribution was calculated from the adsorption branch [17–19].

FTIR spectra were collected on a PerkinElmer Spectrum 65 spectrometer in the mid-infrared range. Surface morphology was examined by field-emission scanning electron microscopy at an accelerating voltage of 20 kV, with images recorded at nominal magnifications of ×300, ×1,000, ×3,000, and ×10,000. Characterization was performed on the final Fe_3O_4/zeolite A composite. Accordingly, the diffraction and microscopy data provide qualitative phase and morphological information, while the final Fe content and spatial distribution of the iron-oxide phase remain unquantified.

3. Results and Discussion

3.1. Powder X-Ray Diffraction

The powder XRD pattern of the Fe_3O_4/zeolite A composite is shown in Figure 1. Intense reflections occurred at 2θ = 7.18°, 10.18°, 12.46°, 16.12°, 21.68°, 24.00°, 27.14°, 29.98°, and 34.20°. In particular, the low-angle reflections at 7.18°, 10.18°, and 12.46°, together with the broader peak sequence, are characteristic of the LTA framework [20,21]. The pattern therefore identifies

LTA as the dominant zeolitic phase obtained from the kaolin-derived synthesis mixture.

A second set of reflections appeared near 30.0°, 35.68°, 43.18°, 57.56°, and 62.72°, corresponding to positions commonly assigned to the (220), (311), (400), (511), and (440) planes of spinel Fe_3O_4 [12, 20]. The feature at approximately 30° overlaps an intense LTA reflection and is not independently diagnostic, whereas the peaks near 35.7°, 43.2°, 57.6°, and 62.7° provide clearer evidence for a spinel iron-oxide contribution. Several weak reflections do not coincide with the principal LTA or magnetite series and may originate from residual minerals in the industrial kaolin or minor secondary aluminosilicate phases.

Taken together, the diffractogram supports coexistence of an LTA-dominant zeolite and a spinel iron-oxide phase. The pattern does not distinguish the Fe^{2+}/Fe^{3+} oxidation-state distribution or provide a quantitative Fe_3O_4 loading. In addition, because an XRD pattern of the unloaded zeolite A was not available for direct comparison, changes in relative crystallinity after loading were not quantified.

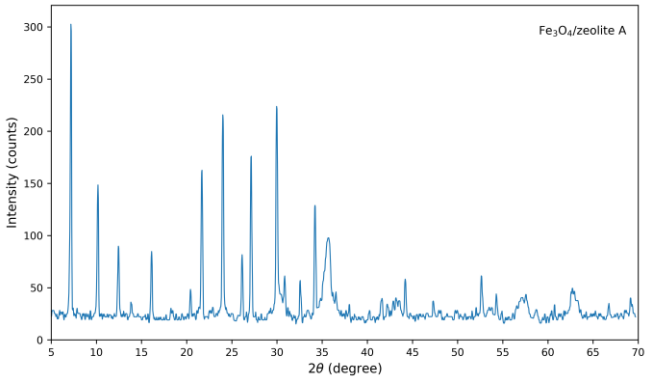


Figure 1. Powder X-ray diffraction pattern of the Fe_3O_4/zeolite A composite recorded with Cu Kα radiation from 5.0 to 69.7° 2θ at a step size of 0.02°.

3.2. Nitrogen Adsorption-Desorption and Textural Properties

Figure 2 presents the N_2 adsorption-desorption isotherm, while Table 2 summarizes the derived textural parameters. The isotherm is predominantly Type II and develops an H3-like hysteresis loop at high relative pressure, a profile associated with particle aggregates and slit-like interparticle voids rather than an ordered mesopore network [18]. Uptake at very low P/P_0 is limited, indicating restricted accessibility of N_2 to part of the intrinsic LTA microporosity at 77 K.

The BET and Langmuir specific surface areas were 18.64 and 20.61 $m^2\ g^{-1}$, respectively. T-plot analysis yielded an external surface area of 9.49 $m^2\ g^{-1}$ and a micropore volume of 0.00426 $cm^3\ g^{-1}$. These values describe the surface accessible to N_2 under the measurement conditions. For cation-containing LTA materials, diffusion through the small pore windows can be restricted at 77 K, so nitrogen-based surface-area analysis may underrepresent the crystallographic micropore space [23, 24].

A total pore volume of 0.03395 $cm^3\ g^{-1}$ was measured near $P/P_0 = 0.99$, close to the BJH adsorption-branch pore volume of 0.03256 $cm^3\ g^{-1}$. The average pore diameter was 7.29 nm, while the dominant BJH radius of 1.29 nm corresponds to a diameter of approximately 2.58 nm. In conjunction with the aggregated morphology observed by FESEM, these mesopore-scale dimensions are most consistent with voids between particles and aggregates rather than uniform intracrystalline mesopores within LTA crystals [18, 24].

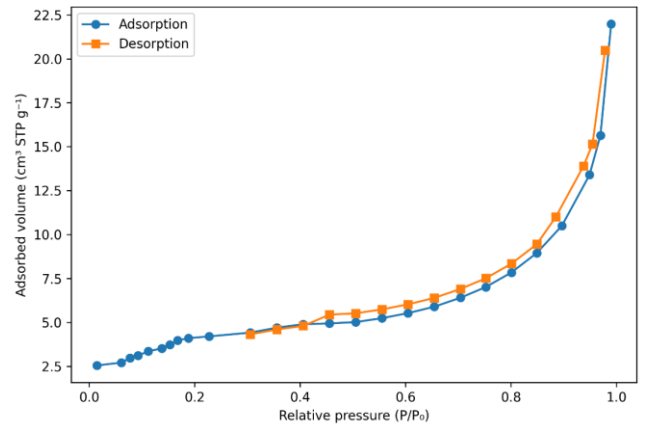


Figure 2. N_2 adsorption-desorption isotherm of the Fe_3O_4/zeolite A composite recorded at 77 K.

Table 2. Textural properties of the Fe_3O_4/zeolite A composite determined by N_2 adsorption-desorption at 77 K.

Textural parameter	Value	Unit
BET specific surface area	18.64	$m^2\ g^{-1}$
Langmuir specific surface area	20.61	$m^2\ g^{-1}$
External surface area[a]	9.49	$m^2\ g^{-1}$
Micropore volume[a]	0.00426	$cm^3\ g^{-1}$
Total pore volume[b]	0.03395	$cm^3\ g^{-1}$
BJH pore volume[c]	0.03256	$cm^3\ g^{-1}$
Average pore diameter	7.29	nm
Dominant BJH pore diameter[c]	2.58	nm

[a] Obtained by t-plot analysis. [b] Determined near $P/P_0 = 0.99$. [c] Calculated from the adsorption branch.

3.3. Fourier-Transform Infrared Spectroscopy

The FTIR spectrum of Fe_3O_4/zeolite A is shown in Figure 3. Bands at 3620 and 1643 cm^{-1} are assigned to O-H stretching and bending of adsorbed water, respectively [20, 21]. A weak feature at approximately 2351 cm^{-1} is attributable to atmospheric CO_2 and was not interpreted as part of the composite structure.

The broad absorption centered at 1037 cm^{-1} arises from asymmetric stretching of the aluminosilicate T-O-T framework (T = Si or Al). Bands at 777 and 629 cm^{-1} are associated with symmetric stretching and external framework vibrations involving Si-O-Si and Si-O-Al linkages, while the feature at 478 cm^{-1} is assigned to framework bending [20, 21]. This set of bands is consistent with the LTA-containing aluminosilicate framework identified by XRD.

The band near 568 cm^{-1} falls within the region reported for double four-membered-ring vibrations of LTA and also overlaps the Fe-O stretching region of magnetite [21,22]. Its position is therefore compatible with contributions from both phases, but it cannot independently establish the oxidation state or abundance of the iron oxide.

A shoulder near 948 cm^{-1} can be associated with terminal T-OH groups, framework defects, or less-condensed aluminosilicate species. Because this feature is not specific to an interfacial Fe-O-Si linkage, no such bond assignment was made. Overall, the FTIR spectrum supports the aluminosilicate framework and is compatible with an iron-oxide contribution in the low-wavenumber region.

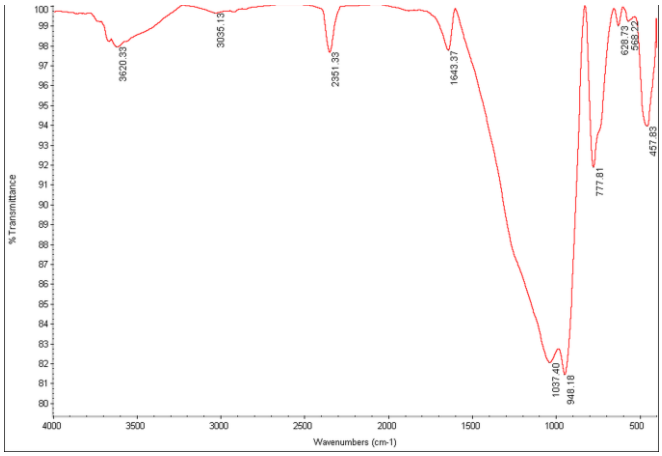


Figure 3. FTIR spectrum of the Fe_3O_4/zeolite A composite showing the principal aluminosilicate bands and the low-wavenumber region where LTA ring vibrations overlap with Fe-O stretching.

3.4. Field-Emission Scanning Electron Microscopy

FESEM images recorded at four magnifications are presented in Figure 4. At low magnification, irregular aggregates with rough surfaces dominate the field of view, with open spaces separating adjacent particles. The larger agglomerates appear to comprise smaller particles brought into contact during composite preparation and drying.

At intermediate magnification, angular, plate-like, and partially faceted particles are distinguishable. Kaolin-derived zeolite A is often reported with cubic or rounded-cubic morphologies [21,25], although aggregation and surface deposition can obscure the outlines of individual crystals. Morphological heterogeneity may also reflect differences in crystal growth or residual aluminosilicate domains inherited from the industrial kaolin.

Fine deposits become visible on several larger particles at higher magnification. Their morphology is compatible with deposition of a second particulate phase during loading, but FESEM contrast alone does not identify its elemental composition; elemental mapping would be required to localize Fe directly [8]. The voids visible between aggregates are far larger than LTA micropores and are therefore interparticle features, consistent with the high-pressure hysteresis in the N_2 isotherm [18].

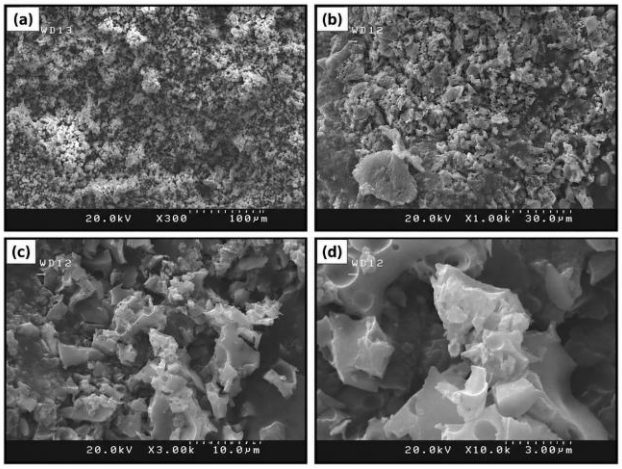


Figure 4. FESEM micrographs of the Fe_3O_4/zeolite A composite at (a) ×300, (b) ×1,000, (c) ×3,000, and (d) ×10,000.

3.5. Oxidative Desulfurization Performance

3.5.1. Operating-Condition Screening

H_2O_2 dosage, H_3PO_4 dosage, composite dosage, reaction temperature, reaction time, stirring speed, and the number of methanol extractions were screened individually. The tested levels and residual sulfur values are reported in Tables S1-S9. Because the screening was conducted one factor at a time and without replicate runs, the data are interpreted descriptively; interaction effects and experimental standard deviations are not available.

Changing the dosage of 33 wt% H_2O_2 solution from 4 to 5 wt% reduced residual sulfur from 150.0 to 105.0 ppmw, while 6 wt% gave 82.5 ppmw. Temperature produced a similar trend: sulfur removal increased from 90.0% at 25 °C to 93.0% at 30 °C and 94.5% at 35 °C. Extending the reaction from 30 to 45 and 60 min yielded removal values of 89.0, 93.0, and 95.0%, respectively. The selected settings of 5 wt% H_2O_2 solution, 30 °C, and 45 min were therefore chosen as a lower-severity operating combination rather than as the individual maxima of the screening ranges.

Composite dosage changed the response only slightly over the tested interval: 0.50, 1.00, and 1.50 wt% produced 93.0, 93.2, and 93.1% sulfur removal, respectively. H_3PO_4 dosages of 1, 2, and 3 wt% gave 89.3, 93.0, and 92.7%, making 2 wt% the highest-performing level among those examined. The absence of a zero-acid run prevents isolation of the H_3PO_4-specific contribution from acidity or non-catalytic peroxide chemistry. Increasing stirring speed from 400 to 500 rpm changed removal from 93.0 to 93.4%. Extraction had a more pronounced effect: one methanol extraction gave 87.0% overall removal, whereas a second extraction raised the value to 93.0%. Because sulfur was not measured between oxidation and the first extraction, the oxidation and first-extraction contributions cannot be quantified separately; the second extraction contributed an additional 6.0 percentage points to the measured overall removal.

3.5.2. Performance at the Selected Condition

At the selected condition, the oxidation stage contained 0.50 wt% Fe_3O_4/zeolite A, 5 wt% of the 33 wt% H_2O_2 solution, and 2 wt% H_3PO_4 and was operated at 30 °C for 45 min and 400 rpm. Two successive extractions with fresh methanol followed. Across this complete sequence, total sulfur decreased from 1500 to 105 ppmw, corresponding to 93.0% overall removal according to Equation (1). The use of real gas condensate retains the complexity of the native hydrocarbon matrix and sulfur distribution [5], although bulk sulfur analysis does not resolve the conversion of individual sulfur species.

The calculated O/S ratio was 10.4, compared with the stoichiometric value of 2 for oxidation of sulfur to the corresponding sulfone. This excess oxidant may compensate for peroxide decomposition and limited utilization in the biphasic reaction environment, but H_2O_2 consumption was not measured. The reported sulfur decrease therefore represents the measured outcome of the applied treatment sequence and does not by itself establish complete oxidation of all sulfur-containing molecules.

3.5.3. Interpretation of the Fe_3O_4/Zeolite A Oxidation-Extraction Sequence

Figure 5 summarizes a chemically plausible oxidation and separation sequence for the Fe_3O_4/zeolite A-H_2O_2-H_3PO_4 system. Magnetite is known to contain Fe^{2+}/Fe^{3+} redox sites that can interact with H_2O_2 [6, 26]. At accessible solid-liquid interfaces, peroxide activation can generate oxidizing species capable of converting organosulfur compounds first to sulfoxides and then to sulfones. In the present composite, this pathway remains a mechanistic interpretation because iron oxidation states, transient oxidizing species, and peroxide consumption were not measured directly.

H_3PO_4 creates an acidic aqueous environment and can alter both peroxide reactivity and the surface chemistry of iron oxides. Within the tested 1-3 wt% range, the best response occurred at 2 wt%, but the absence of a zero-acid control precludes assignment of the improvement specifically to acid promotion. The LTA support provides an external aluminosilicate surface on which Fe_3O_4 can be deposited; given the small LTA pore windows, bulky petroleum sulfur compounds are expected to interact predominantly with liquid-accessible external regions rather than the intrinsic micropore network.

Oxidation increases the polarity of organosulfur species but does not itself remove them from the hydrocarbon phase. Methanol preferentially extracts the more polar oxidation products, and replacement with fresh solvent in the second stage restores the concentration driving force for transfer [27]. Consistent with this sequence, the second methanol extraction increased overall sulfur removal from 87.0 to 93.0%. The available measurements quantify the performance of the combined process but not the separate shares of catalytic oxidation, non-catalytic oxidation, adsorption, and the first extraction.

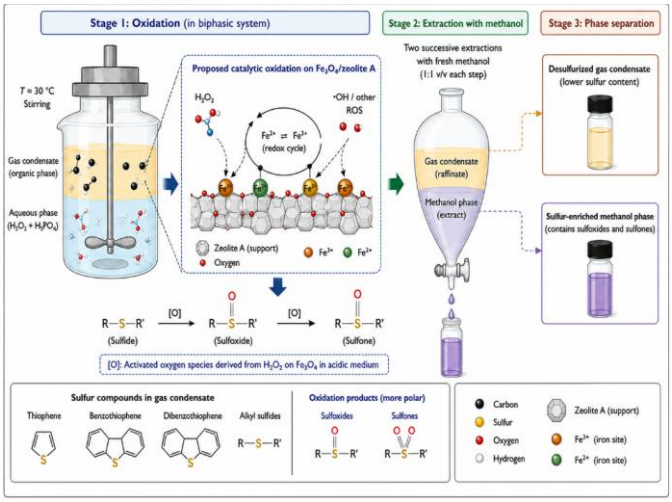


Figure 5. Proposed oxidation and extraction sequence for sulfur removal from real gas condensate using Fe_3O_4/zeolite A, H_2O_2, and H_3PO_4. The reactive intermediates and active-site assignments are schematic and were not identified directly.

3.5.4. Comparison with Reported Oxidative Desulfurization Systems

Direct ranking of ODS studies by removal percentage is unreliable because feed composition, starting sulfur level, oxidant chemistry, catalyst dosage, mixing, temperature, and downstream extraction differ substantially. Pouladi et al. reported 95.56% sulfur removal from sour natural gas condensate using H_2SO_4, HNO_3, and NO_2 under high-shear mixing [5]. Although the feed class is comparable to the present study, the oxidizing medium and hydrodynamic regime are fundamentally different.

Using a model fuel, Kargar et al. achieved complete dibenzothiophene conversion over Fe_3O_4/ZIF-8/TiO_2 with tert-butyl hydroperoxide at 80 °C for 6 h [6]. Such compound-specific conversion cannot be equated directly with total-sulfur removal from a real petroleum matrix. Mokhtari et al. reported approximately 99.9% sulfur removal from hydrotreated diesel over MoO_3/silica gel at 45 °C for 90 min followed by acetonitrile extraction [28]. These comparisons place the present result within the ODS literature while preserving differences in feedstock and process boundaries.

The present treatment combines a kaolin-derived LTA support, nominal 6 wt% Fe_3O_4 addition, aqueous H_2O_2, 30 °C oxidation, and a 45 min reaction period. Its principal process burden is the use of two fresh methanol volumes, each equal to the initial feed volume. Scale-up would therefore require solvent recovery together with quantification of hydrocarbon entrainment, peroxide utilization, residual solvent, and phase-separation efficiency.

3.5.5. Analytical Scope and Catalyst Stability

The dataset establishes the phase characteristics, textural properties, and morphology of the final composite and quantifies total sulfur before and after the complete treatment sequence. It does not contain blank experiments with H_2O_2/H_3PO_4 alone, zeolite A alone, Fe_3O_4 alone, or extraction alone. Consequently, the individual contributions of the support, iron-oxide phase, non-catalytic oxidation, adsorption, and solvent extraction cannot be separated quantitatively from the present measurements.

No recycle series, iron-leaching measurement, or post-reaction characterization

was included in the experimental program. Catalyst stability, retention of the deposited iron phase, and performance over repeated cycles therefore remain unquantified. Further process assessment would also require replicate measurements, hydrocarbon yield and loss to methanol, residual methanol, solvent-recovery efficiency, and compound-specific sulfur analysis. These measurements would define catalyst-specific activity and process durability beyond the overall sulfur-removal response reported here.

4. Conclusions

Template-free hydrothermal treatment converted Iranian kaolin to an LTA-dominant zeolitic material that served as the support for a nominal 6 wt% Fe_3O_4 addition. The final composite retained the characteristic low-angle reflections of LTA and displayed additional XRD peaks consistent with a spinel iron-oxide phase. Nitrogen adsorption at 77 K gave a BET specific surface area of 18.64 $m^2\ g^{-1}$, an external surface area of 9.49 $m^2\ g^{-1}$, and a total pore volume of 0.03395 $cm^3\ g^{-1}$. The H3-like high-pressure hysteresis and FESEM morphology indicate that much of the measured mesopore-scale volume is associated with interparticle spaces.

For a real gas condensate containing 1500 ppmw sulfur, the selected oxidation condition used 0.50 wt% composite, 5 wt% of 33 wt% H_2O_2 solution, 2 wt% H_3PO_4, 30 °C, 45 min, and 400 rpm, followed by two methanol extractions at a 1:1 solvent-to-initial-feed volume ratio per stage. Residual sulfur was 105 ppmw, giving 93.0% overall removal. Higher H_2O_2 dosage, temperature, or reaction time produced modest additional reductions in residual sulfur, while increasing the composite dosage above 0.50 wt% had little effect within the screened range.

The measured response belongs to the combined oxidation-extraction process. A magnetite-assisted peroxide pathway is chemically plausible, but the present data do not resolve iron oxidation states, active intermediates, or the catalyst-specific share of sulfur removal. Quantitative Fe analysis, controlled blank experiments, replicate measurements, iron-leaching tests, and recycle studies would provide the next level of evidence needed to separate composition, mechanism, and durability effects.

Author Contributions

All authors contributed equally to the conception, preparation and writing of this manuscript.

Conflict of Interest

The authors, while observing publication ethics in the referencing, declare the absence of interest of conflict.

Acknowledgement

We sincerely thank the reviewers for their valuable and constructive comments, which helped us improve the quality of this manuscript.

AI-Assisted

The authors retain full responsibility for the accuracy, originality, integrity, legality, and ethical compliance of all text, data, tables, figures, analyses, references, and conclusions, and have verified all AI-assisted outputs. Any fabrication, falsification, manipulation, plagiarism, copyright infringement, or other misuse of AI remains solely the responsibility of the authors and does not transfer or diminish their accountability for the published work.

References

[1] R. Shafi, G. J. Hutchings, *Catalysis Today*, 2000, **59(3–4)**, 423–442.

[2] M. Jafari, M. R. Khosravi-Nikou, M. Motavasel. *Journal of Environmental Economics and Chemical Processes*, 2025, ***2*(2)**, 39-45. doi: 10.22034/jeecp.2025.735010.

[3] L. Zarin, J. Saien. *Journal of Environmental Economics and Chemical Processes*, 2025, ***2*(2)**, 47-51. doi: 10.22034/jeecp.2025.735011.

[4] F. Boshagh, M. Rahmani, K. Rostami, M. Yousefifar, *Energy & Fuels*, 2022, **36(1)**, 98–132.

[5] B. Pouladi, M.A. Fanaei, G. Baghmisheh, *Journal of Cleaner Production*, 2019, **209**, 965–977.

[6] M. J. Bradley, P.G. Tratnyek, *ACS Earth and Space Chemistry*, 2019, **3(5)**, 688–699.

[7] R. Liu, S. Dou, M. Yu, R. Wang, *Journal of Cleaner Production*, 2017, **168**, 1048–1058.

[8] H. Kargar, M. Ghahramaninezhad, M.N. Shahrak, S.S. Balula, *Microporous and Mesoporous Materials*, 2021, **317**, 1109921-9.

[9] W. Shan, T. Yu, B. Wang, J. Hu, Y. Zhang, X. Wang, Y. Tang, *Chemistry of Materials*, 2006, **18(14)**, 3169–3172.

[10] M. Jafari, T. Mohammadi, M. Kazemimoghadam, *Ceramics International*, 2014, **40(8)**, 12075–12080.

[11] W. R. Lim, C.-H. Lee, S.-Y. Hamm, *Materials Chemistry and Physics*, 2021, **261**, 1242301-11.

[12] M. Gougazeh, J. Ch. Buhl, *Journal of the Association of Arab Universities for Basic and Applied Sciences*, 2014, **15(1)**, 35–42.

[13] S. Chandrasekhar, P. N. Pramada, *Microporous and Mesoporous Materials*, 2008, **108(1–3)**, 152–161.

[14] M. Mascolo, Y. Pei, T. Ring, *Materials*, 2013, **6(12)**, 5549–5567.

[15] ASTM International, ASTM D4294-24, Standard Test Method for Sulfur in Petroleum and Petroleum Products by Energy-Dispersive X-ray Fluorescence Spectrometry, (2024). https://store.astm.org/d4294-24.html.

[16] S. Vedachalam, P. Boahene, A. K. Dalai, *Energy & Fuels*, 2020, **34(12)**, 15299–15312.

[17] E.P. Barrett, L.G. Joyner, P.P. Halenda, *Journal of the American Chemical Society*, 1951, **73(1)**, 373–380.

[18] M. Thommes, K. Kaneko, A.V. Neimark, J.P. Olivier, F. Rodriguez-Reinoso, J. Rouquerol, K.S.W. Sing, *Pure and Applied Chemistry*, 2015, **87(9–10)**, 1051–1069.

[19] S. Brunauer, P. H. Emmett, E. Teller, *Journal of the American Chemical Society*, 1938, **60(2)**, 309–319.

[20] S. Salimkhani, K. Siahcheshm, A. Kadkhodaie, H. Salimkhani, *Materials Chemistry and Physics*, 2021, **271**, 1249571-11.

[21] A. R. Loiola, J. C. R. A. Andrade, J. M. Sasaki, L. R. D. Da Silva, *Journal of Colloid and Interface Science*, 2012, **367(1)**, 34–39.

[22] Y. Hadadian, H. Masoomi, A. Dinari, C. Ryu, S. Hwang, S. Kim, B.K. Cho, J.Y. Lee, J. Yoon, *ACS Omega*, 2022, **7(18)**, 15996–16012.

[23] Y. S. Bae, A.Ö. Yazaydın, R.Q. Snurr, *Langmuir*, 2010, **26(8)**, 5475–5483.

[24] S. M. P. De Lucena, J. C. A. Oliveira, D. V. Gonçalves, L. M. O. Lucas, P. A. S. Moura, R. G. Santiago, D. C. S. Azevedo, M. Bastos-Neto, *Industrial & Engineering Chemistry Research*, 2022, **61(5)**, 2268–2279.

[25] L. Ayele, J. Pérez-Pariente, Y. Chebude, I. Díaz, *Microporous and Mesoporous Materials*, 2015, **215**, 29–36.

[26] X. Wang, W. Liu, J. Qin, L. Lei, *Industrial & Engineering Chemistry Research*, 2020, **59(5)**, 2192–2202.

[27] F. Al-Shahrani, T. Xiao, S.A. Llewellyn, S. Barri, Z. Jiang, H. Shi, G. Martinie, M.L.H. Green, *Applied Catalysis B: Environmental*, 2007, **73(3–4)**, 311–316.

[28] B. Mokhtari, A. Akbari, M. Omidkhah, *Energy & Fuels*, 2019, **33(8)**, 7276–7286.